Check for updates

Group-VIII transition metal boride as promising hydrogen evolution reaction catalysts†

Guang-Feng Wei,[*a] Ling-Ran Zhang[a] and Zhi-Pan Liu [iD] [*b]

Searching for alternative catalysts for hydrogen evolution reaction (HER) under acidic conditions has been a major challenge in chemistry. Herein, we demonstrate that it is now feasible to identify unprecedented transition metal boride phases that are both stable and active for HER *via* stochastic global potential energy surface scanning. We show that B alloying alters the most stable crystal phase from face-centered (fcc) to hexagonal close packing (hcp) for both Pd and Rh. In particular, Pd_2B, the thermodynamically most stable Pd boride with the highest B content, is predicted to exhibit an ultra-high intrinsic HER activity, ~ 2 orders of magnitude higher than that of Pt nanoparticles at 0 V *vs.* NHE. The group VIII transition metal boride thus represents a promising HER catalyst to replace conventional Pt catalysts.

Introduction

Pt metal is a key material for catalyzing HER,[1,2] ranked as the highest activity metal[3,4] in the periodic table. While HER can occur in both acidic ($2H^+ + 2e^- \rightarrow H_2$) and alkaline conditions ($2H_2O + 2e^- \rightarrow H_2 + 2OH^-$), the acidic condition is generally pursued for its higher activity, apparently due to the fast proton (or adsorbed H) supply and there being no need for additional water splitting on catalyst. The high activity and long-term stability under acidic conditions are two outstanding properties of Pt, which could all boil down to the unique Pt–H interaction,[5,6] being modest for H binding on surfaces but strongly positive in bulk. It is thus a major challenge in chemistry to search for materials that can achieve the similar H-surface/bulk interaction as Pt, which is the key step towards economic, highly active and stable catalysts for acidic HER.

Recent theory has shown that most of the group VIII transition metals can, in fact, achieve a modest H/surface binding as the H coverage on surface builds up at low potentials. Their lower activity than Pt is more related to the undesirable high affinity of H in metal bulk, which leads to the dynamic H

penetration into the bulk and thus the loss of active sites. For example, Pd has the H/surface binding strength similar to Pt (difference of ~ 0.05 eV[7]), but the subsurface Pd-hydride can form readily, resulting in surface deformation and activity reduction.[8,9] Two promising strategies were most utilized in literatures to improve the stability of non-Pt metal catalysts under acidic conditions: (i) to support metal particles on active materials and (ii) to alloy transition metal with main group elements, such as P,[10–16] S.[17–23] The high HER activity was reported for ~ 1 nm sized Ru[24] particles supported on C_2N sheet, which can catalyze HER with an overpotential of 13.5 mV at 10 mA cm^{-2} (*cf.* 16 mV for Pt/C) under acidic condition. For alloys, the highest activity known so far is still 12 mV lesser (RuP_2 catalyst) compared to that of Pt catalyst.[12] Since the bulk alloy catalysts are more attractive for generating large-scale industrial catalyst, it is of significance to ask how to identify transition metal main-group element alloys with high activity. However, our current knowledge on these alloys is far short of expectation: the structure and the thermodynamic stability of alloys are notoriously hard to determine, not even to mention their activity and stability under HER conditions.

Herein, we present a systematic bottom-up approach to search for non-Pt HER catalyst with desirable high thermodynamic stability and high HER activity. Our method involves state-of-the-art global optimization techniques to explore the potential energy surface (PES) of alloys, followed by the quantitative evaluation of HER activity and stability at the solid–liquid interface under electrochemical conditions. We demonstrate this by using Pd_xB and Rh_xB systems. We find that B alloying significantly increases the metal HER activity and stability. In particular, Pd_2B (*i.e.* 0.33 B atomic content), a hcp phase metal alloy is identified as the thermodynamically most stable PdB alloy, which also achieves higher intrinsic HER activity than Pt nanoparticles.

[a] *Shanghai Key Laboratory of Chemical Assessment and Sustainability, School of Chemical Science and Engineering, Tongji University, Shanghai 200092, China. E-mail: weigf@tongji.edu.cn*

[b] *Collaborative Innovation Center of Chemistry for Energy Material, Shanghai Key Laboratory of Molecular Catalysis and Innovative Materials, Key Laboratory of Computational Physical Science (Ministry of Education), Department of Chemistry, Fudan University, Shanghai 200433, China. E-mail: zpliu@fudan.edu.cn*

† Electronic supplementary information (ESI) available: GM structures of Pd_xB, details about the relative formation energy diagram and the results of Rh_xB, surface phase diagrams and H adsorption structures on Pd_xB, the reaction profiles, polarization curves from theory and the detail results of subsurface H formation. See DOI: 10.1039/c8cp05079a

27752 | *Phys. Chem. Chem. Phys.*, 2018, **20**, 27752–27757

This journal is © the Owner Societies 2018

Computational details

Density functional theory (DFT) calculations

All stochastic surface walking (SSW) calculations were performed in combination with the periodic DFT calculations as implemented in the plane wave code VASP.[25] The projected augmented wave (PAW)[26,27] pseudo-potentials were utilized to describe the ionic core potential. The plane-wave kinetic energy cutoff of 400 eV was used and the exchange–correlation functional utilized was at the generalized gradient approximation level GGA-PBE.[28] The Monkhorst–Pack scheme with a k-point separation length of 0.04 Å^{-1} was utilized for sampling the first Brillouin zone.

The reaction modelling for HER was carried out by SIESTA package[29,30] with Troullier–Martins norm conserving pseudo-potentials.[31] The exchange–correlation functional utilized was at the generalized gradient approximation level, known as GGA-PBE.[28] The optimized double-ζ plus (DZP) polarization basis set with extra diffuse function was employed for metal. The orbital-confining cutoff was determined from an energy shift of 0.010 eV. The energy cutoff for the real space grid used to represent the density was set as 150 Ry. The Quasi-Newton l-BFGS method is used for geometry relaxation until the maximal force on each degree of freedom is less than 0.05 eV Å^{-1}. The accuracy of the calculated energetics was examined by bench-marking the results from SIESTA with those from the plane-wave methodology and the difference in adsorption energy is generally below 0.05 eV for H.[32] To correct the zero-point energy for reaction barrier, the vibrational frequency calculations were performed *via* the finite-difference approach. Transition states (TSs) of the catalytic reaction were searched using the Constrained-Broyden-based TS-searching methods[33,34] and the Double-Ended Surface Walking method.[35]

To derive the free energy reaction profile, we first obtain the reaction energy of each step (strictly speaking, Helmholtz free energy change (ΔF) at 0 K, 0 bar) that is directly available from DFT total energy (ΔE) after the ZPE correction. For elementary surface reactions without involving the adsorption/desorption of gaseous or liquid molecules, ΔF at 0 K, 0 bar is a good approximation of the Gibbs free energy (ΔG) as the contributions of temperature T and pressure p at the solid phase are small. To compute the free energy change ΔG of elementary reactions involving gaseous or liquid molecules, such as hydrogen and water, it is essential to take into account the large entropy term at 298 K. We utilize the standard thermodynamic data[36] to obtain the temperature and pressure contributions for G of the aqueous H_2O and gaseous H_2, which are -0.57 eV (the entropy contribution is -0.22 eV in solution) and -0.31 eV compared to the total energy of the corresponding free molecule (E, 0 K), respectively.[37]

Stochastic surface walking (SSW) sampling method

In SSW simulation, we used the basic structure search module of SSW to explore the PES of metal borides in a series of supercells, up to 24-atom (*e.g.* Pd_{24}, $Pd_{16}B_2$, Pd_8B_{16}) per super-cell. For each composition, we started from one single phase (typically the random structures) and let SSW explore all the likely phases. The Metropolis Monte Carlo scheme was utilized

to accept or reject a newly found structure in every SSW step. All minima visited in SSW were recorded and analyzed according to their geometry. This eventually produced a database containing a large number of possible phases. In this study, the Gaussian width ds was set as 0.6, the number of Gaussian was 10.

To identify the global minimum structure of Pd_xB (see Fig. S1, ESI†), we set the temperature utilized in Metropolis Monte Carlo to 3000–6000 K. The higher temperature was used to verify the obtained global minimum structure. In the SSW search, for each Pd_xB, we performed up to 100 parallel runs and more than 1200 distinct minima were collected, from which the most stable configuration was obtained. We verified the most stable configuration by performing new SSW runs until no stabler configuration was identified at the stage of verification.

Theoretical approach for studying electrochemical systems

The solid/liquid interface was described by using the periodic continuum solvation model based on the modified Poisson–Boltzmann equation (CM-MPB), which can take into account the long-range electrostatic interaction due to the solvation of electrolyte.[17,38,39] The DFT/CM-MPB method has been utilized to calculate the electro- and photo-catalytic reactions at the solid–liquid interfaces[17,38,39] and compute the fundamental properties of metal surfaces in solution such as the zero charge potential and the differential capacitance, where the calculated values show good agreement with the available experimental data.[40]

For reactions involving the release of proton and electron, the reaction energy can be computed by referencing to the normal hydrogen electrode (SHE) in a manner proposed by the Bockris and Khan[41] and Nørskov *et al.*[42] This is governed by $G_{proton+electron} = G(1/2H_2) - neU$ where e represents the transfer electron, n is the number of electrons, and U is the electro-chemical potential *vs.* SHE.

Results and discussion

Our investigation starts by predicting the phase diagram of the Pd- and Rh-B alloys using first principles stochastic surface walking (SSW) global optimization.[43,44] A set of alloys covering full range compositions, including PdB_2, PdB, Pd_2B, Pd_3B, Pd_5B, Pd_8B and $Pd_{11}B$ for Pd_xB and RhB_3, RhB_2, RhB, Rh_2B, Rh_7B_3, Rh_3B, Rh_5B and $Rh_{11}B$ for Rh_xB, have been investigated with the aim to find the most stable structure (*i.e.* the global minimum, GM) and reveal the PES information (*e.g.* glassy or non-glassy). Because the thermodynamic trend for Rh_xB is very similar to that for Pd_xB, herein, we focus on the results of Pd_xB, as summarized in Fig. 1a (also see ESI,† Fig. S1). Fig. 1a plots the relative formation energy (ΔE) of Pd_xB alloy against boron content, where the ΔE is defined as the energy change in alloy formation from pure Pd and B phases (more details and the results of Rh_xB are included in ESI,† Fig. S2). Fig. 1a clearly shows that with the increase in B content, ΔE first decreases (from Pd to Pd_2B) and then increases (from Pd_2B to B). Only $Pd_{11}B$, Pd_8B, Pd_5B, Pd_3B and Pd_2B are stable alloys from the convex hull (disproportionation to neighbouring

This journal is © the Owner Societies 2018

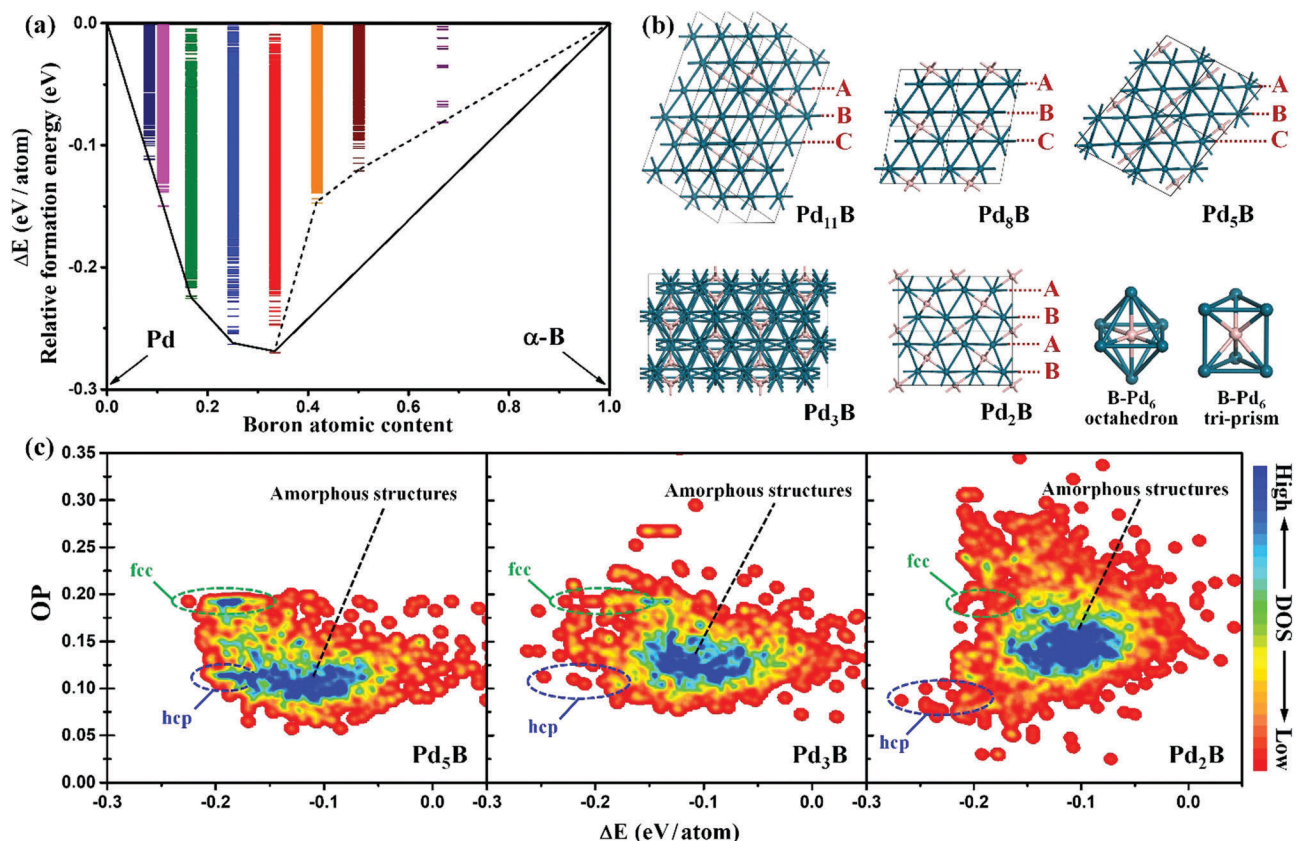*Phys. Chem. Chem. Phys.*, 2018, **20**, 27752–27757 | 27753

Fig. 1 (a) The relative formation energy (eV per atom) of Pd borides with respect to Pd metal (fcc) and α-B. The energy spectrum for all configurations of each composition is plotted as a colour bar and the convex hull outlined by the solid lines indicates the thermodynamically stable phases; (b) the most stable structures of the thermodynamically stable compositions and two typical Pd–B bonding pattern. The red dashed lines indicate the Pd sublattice. (c) PES contour plot for Pd_5B, Pd_3B and Pd_2B minima phases from SSW sampling. The x-axis is the relative formation energy and the y-axis is the Steinhardt-type order parameter(OP).[46] The green/blue dashed circles show the phases with fcc/hcp Pd sublattice.

compositions is not favoured energetically). Pd_2B is predicted to be the stable alloy with the highest boron content. Only three major Pd_xB alloys, i.e. Pd_3B, Pd_5B_2 and Pd_2B were ever reported in experiments[45] and indeed, no B content is higher than 0.33.

In the following, we will elaborate the structure and PES evolution from Pd to Pd_2B.

Structure evolution of Pd_xB

The GM crystal structures for Pd_xB are shown in Fig. 1b. From Pd to Pd_2B, the Pd sublattice in the GM structure transforms from fcc packing to hcp. Specifically, the $Pd_{11}B$, Pd_8B and Pd_5B have the fcc Pd sublattice while Pd_2B has the hcp Pd sublattice. In these structures, B always prefers to distribute uniformly in the interstitial O_h sites (i.e. forming a B-Pd_6 octahedron). Pd_3B appears as a transition composition from the fcc to the hcp. The GM of Pd_3B has a Pd sublattice with $Pnma$ symmetry and B is located in the middle of a tri-prism Pd_6. Being only 9 meV per atom less stable than the GM, the second lowest minima of Pd_3B (Pd_3B_{SLM}) has an hcp–fcc mixed structure ($R\bar{3}m$) with 1/3 of fcc and 2/3 of hcp in the lattice.

Global PES

To have an overview of the global PES of Pd_xB, we construct the contour map of the PES for Pd_5B, Pd_3B and Pd_2B in Fig. 1c

using all the distinct minima from SSW, where ΔE of each structure is plotted against the Steinhardt-type order parameter (OP)[46] of Pd sublattice with the degree L = 4 (by definition, OP = 0.09 for perfect hcp metal and 0.19 for fcc metal). The color in the map represents the density of states (DOS) of minima. From Fig. 1c, we can see that (i) all Pd_xB do have both the fcc and hcp phases (as circled in figures), but with the increase in B contents, the preference in energy shifts from the fcc to the hcp. (ii) the structure variety substantially increases at high B content, as reflected by the large increase in the area of the map. The OP of Pd_5B, similar to pure Pd, is within 0.05–0.2, but it spans from 0.02 to 0.35 in Pd_2B. This indicates that Pd_2B has a higher structure flexibility with more Pd bonding environment: Pd sublattice is able to deviate significantly from the close packing ground state at high energies, which implies a strong glass forming ability when quenched from high temperatures.

HER catalytic kinetics

Knowing the thermodynamic stable forms, i.e. all convex points in Fig. 1a, we can then assess their catalytic HER performance from DFT. While there are two likely reaction routes for HER, i.e. Heyrovsky (surface H reacting with proton) and Tafel (surface H coupling reaction $H^* + H^* \rightarrow H_2$), our previous study has

shown that Tafel mechanism is a key pathway for good HER catalysts, such as Pt, where the surface H coverage is high.[6] The free energy barrier for Tafel route on boride surfaces, *i.e.* the close-packing surfaces as the model (Pd(111), Pd$_8$B(010), Pd$_5$B($\bar{1}$02), Pd$_3$B$_{SLM}$(010), Pd$_2$B(010), Rh(111), Rh$_2$B(100) and RhB(001)) at 0 V *vs.* NHE, is thus taken as the measure to compare the activities of different catalysts.

To study the Tafel reaction, one needs to know first the equilibrium surface H coverage under reaction conditions, where the adsorbed H equilibrates with solvated protons in electrolyte. Using DFT calculations and thermodynamic analyses (see ESI,† Fig. S3 and also in ref. 47), we have determined the H adsorption free energy ΔG_H, structures and the equilibrium coverage at 0 V. The ΔG_H at the low H coverage (0.2–0.25 ML) are summarized in Table S1 (ESI†). We found that with the increase in B content, ΔG_H slightly increases at first and then rapidly decreases. The former is due to the surface relaxation (surface tensile strain) after B insertion, and the latter is caused by a typical bonding competition where the existing Pd–B bonds weakens the Pd–H bonding. As for the most favourable adsorption structure, we found that the adsorbed H generally prefers to adsorb at the three-fold hollow site, bonding with three metal atoms, where no subsurface B directly beneath the hollow site is present, as shown in ESI,† Fig. S4. Evidently, a too-close contact (<2 Å) between H and B is thermodynamically prohibited. This effect leads to the gradual decrease of equilibrium H coverage as the B contents increase in Pd(Rh)$_x$B materials. Fig. 2a shows the calculated H* coverage at 0 V for different materials. It can be seen clearly that the H coverage drops from 1 to 0.25 monolayer (ML) in Pd$_x$B series and from 1 to 0.5 ML in Rh$_x$B series.

Next, we follow the Tafel mechanism and investigate the kinetics for two surface H coupling to form H$_2$ molecule. Fig. 2b and c show the computed free energy barriers (ΔG_a) for H coupling (the reaction profiles are detailed in ESI,† Fig. S5) and the initial states (ISs) and transition states (TSs) on the representative surfaces, Pd(111) and Pd$_2$B(010). The Tafel reaction on these surfaces shows a great similarity with that on Pt(111). Starting from the equilibrium H coverage condition where all Hs are at the hollow sites, one additional H comes from solution (proton) to get adsorbed (a Volmer step). This additional H then reacts with the nearby hollow site H to achieve the TS. At the TS, the H–H distance is 0.8–1.0 Å, forming a [H–H] complex near a top site. It is interesting that the distances between the reacting Hs at TSs are almost the same (Pd: 0.83 Å and Pd$_2$B: 0.84 Å), while ΔG_a on Pd$_2$B is much lower than that on Pd. In fact, as shown in Fig. 2b, from pure Pd to Pd$_2$B, with the increase in B content, ΔG_a decreases rapidly from 0.77 eV to 0.35 eV. Similarly, the ΔG_a on Rh$_2$B and RhB (being 0.35 and 0.41 eV, respectively) are also much lower than that on Rh(111) (0.78 eV). Moreover, as shown in Fig. S5 (ESI†), the free energy change (ΔG) of H* + H* → H$_{2(g)}$ (corresponding to realistic coverages at 0 V) on Pd(111) and Rh(111) are 0.28 and 0.34 eV, respectively. The ΔG of the same reaction on Pd- and Rh-B surfaces reduce to 0.05–0.13 eV. These results indicate that the B alloying significantly boosts the HER activity.

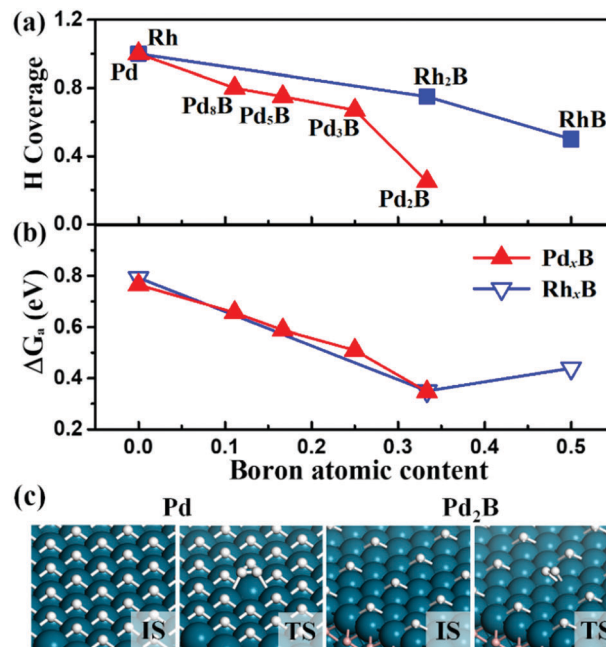To confirm whether the Heyrovsky mechanism may also contribute to HER activity of Pd$_x$B surfaces, we examined

Fig. 2 (a) The equilibrium surface H coverage on Pd(111), Rh(111) and Pd–B, Rh-B alloys. (b) The free energy barriers (ΔG_a) of H–H coupling. (c) The structure snapshots of the initial states (ISs) and transition states (TSs) of H–H coupling reaction on Pd and Pd$_2$B surface. White/cyan/pink balls: H/Pd/B atom.

reaction barrier of the Heyrovsky step (H$^+_{(aq)}$ + H* → H$_2$) on Pd$_2$B(010), which has the lowest equilibrium surface H coverage (0.25 ML). We found that the reaction barrier of Heyrovsky mechanism is 0.43 eV on Pd$_2$B(010), which is 0.08 eV higher than that of Tafel mechanism, suggesting that the Tafel pathway is at least one order of magnitude more important than Heyrovsky pathway. For other Pd$_x$B, the equilibrium surface H coverage is higher than 0.25 ML (as shown in Fig. 3) and thus should also prefer the Tafel mechanism.

Our previous study has shown that Tafel reaction barrier on Pt 1 nm nanoparticles is as low as 0.48 eV,[5] which is 0.3 eV lower than that on Pd(111), but this value is still 0.13 eV higher than that on Pd$_2$B. Compared to the Pt nanoparticles, the exchanged current density on Pd$_2$B can be 2 orders higher at ambient condition according to microkinetics. This would lead to the HER overpotential on Pd$_2$B reaching 0.25 mV at the current density of 30 mA cm^{-2} (see ESI,† Fig. S6), which is much smaller than that of the commercial Pt/C (28 mV).

Naturally, it is interesting to wonder why Pd$_2$B possesses a superior catalytic ability. In Fig. 3, we have compared the total (Fig. 3a) and projected (Fig. 3b and c) density of states (DOSs) for HER on Pd and Pd$_2$B at the IS and the TS. Fig. 3 shows that the presence of B introduces new peaks at −8 to −10 eV in the total DOS, being mainly B 2s states. While both Pd and Pd$_x$B exhibit clear metallic characteristics, the total DOS around Fermi levels (E_f) becomes much smaller for Pd$_x$B, which can be attributed to the hybridization of Pd 4d with B 2p orbitals. We then focus on the reacting H during HER. We found that the Pd–H bonding peaks projected onto the 1s orbital of
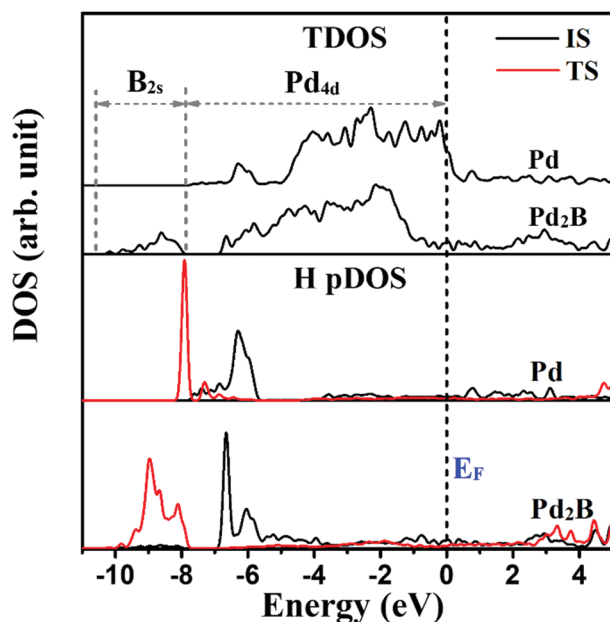
Fig. 3 Total density of states (TDOSs) (top panel) and projected density of states (pDOSs) on to the 1s orbitals of the reacting H atoms (middle and bottom panels) for the H–H coupling reactions at 0 V on Pd(111) and Pd$_2$B(010). The energy levels are with respect to the Fermi levels (E_f).

adsorbed H on Pd(111) and Pd$_2$B(010) are quite similar at the ISs, both around −7.8 to −5 eV. At the TSs, these Pd–H bonding peaks shift to the lower energy regions, reflecting the evolution of nascent [H–H] bonding. In particular, at the TS for HER on Pd(111), the Pd–H bonding peaks diminish and a sharp large peak appears at ∼−8 eV. Moreover, the TS for HER on Pd$_2$B(010) behaves quite differently: while the original Pd–H bonding peaks also disappear, the new H bonding peaks emerge at much lower energies and become broadened, centering around −9 eV. This is caused by the additional resonance between B 2s states and the [H–H] TS complex mediated by the surface Pd. As shown in Fig. 4, the electronic wavefunction contour plot shows the interaction between B states and the [H–H] TS complex as mediated by the surface Pd. The presence of subsurface B thus helps to stabilize the TS complex particularly.
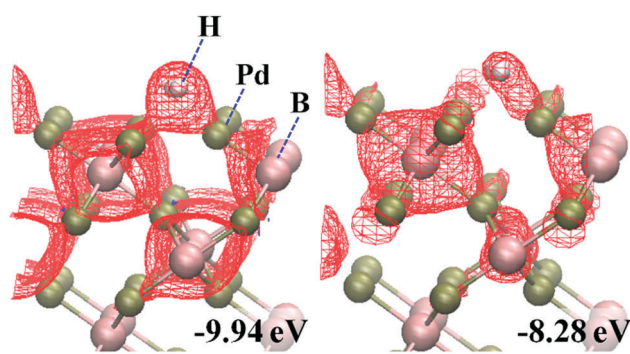

Fig. 4 The 3D electronic wavefunction contour plots at the TS of H–H coupling on Pd$_2$B(010). The energies referred to as E_f are labelled in the lower right corner.

Indeed, by removing the B atom directly beneath the [H–H] TS complex, we have recalculated the HER energetics and found that the reaction barrier of H–H coupling is as high as 0.9 eV. One can therefore conclude that not only the thermodynamic stability of the crystal phases but also B alloying significantly influence the HER kinetics *via* a unique B-metal-[H–H] interaction in HER.

Finally, we also evaluated the stability of Pd- and Rh-boron alloys by calculating the energy cost for the subsurface H formation (ΔG_{sub}). While ΔG_{sub} for pure Pd is almost thermo-neutral (∼0.02 eV) at 0 V, ΔG_{sub} for Pd$_2$B and RhB are found to be strongly endothermic, being 0.74 and 0.97 eV, respectively, which are close to the values for Pt (ΔG_{sub} = 0.94 eV on Pt(111), also see ESI,† Table S2 and Fig. S7 for details). This implies that Pd$_2$B and RhB are highly stable under HER condition. Evidently, the high concentration of subsurface B blocks the penetration of surface H that renders the high stability of the alloy.

Conclusions

In this study, we present a systematic bottom-up approach to search for acidic HER catalyst with high thermodynamic stability and high HER activity. We show that B doping systematically increases the metal HER activity. In particular, Pd$_2$B, the thermo-dynamically most stable Pd boride, is predicted to exhibit an ultra-high intrinsic HER activity, ∼2 orders magnitude higher than that of Pt nanoparticles. These quantitative evidences from the first principles PES data suggest that the alloying of transition metal with boron opens a new paradigm for active and stable HER catalysts.

Conflicts of interest

There are no conflicts to declare.

Acknowledgements

Notes and references

1 V. R. Stamenkovic, B. S. Mun, M. Arenz, K. J. J. Mayrhofer, C. A. Lucas, G. Wang, P. N. Ross and N. M. Markovic, *Nat. Mater.*, 2007, **6**, 241.
2 J. R. McKone, E. L. Warren, M. J. Bierman, S. W. Boettcher, B. S. Brunschwig, N. S. Lewis and H. B. Gray, *Energy Environ. Sci.*, 2011, **4**, 3573.
3 J. K. Norskov and C. H. Christensen, *Science*, 2006, **312**, 1322.
4 Z. W. Seh, J. Kibsgaard, C. F. Dickens, I. B. Chorkendorff, J. K. Norskov and T. F. Jaramillo, *Science*, 2017, **355**, 146.
5 G. F. Wei and Z. P. Liu, *Chem. Sci.*, 2015, **6**, 1485.
6 Y. H. Fang, G. F. Wei and Z. P. Liu, *J. Phys. Chem. C*, 2013, **117**, 7669.

27756 | *Phys. Chem. Chem. Phys.*, 2018, **20**, 27752–27757

This journal is © the Owner Societies 2018

7 J. K. Norskov, T. Bligaard, A. Logadottir, J. R. Kitchin, J. G. Chen and S. Pandelov, *J. Electrochem. Soc.*, 2005, **152**, J23.

8 E. C. H. Sykes, L. C. Fernandez-Torres, S. U. Nanayakkara, B. A. Mantooth, R. M. Nevin and P. S. Weiss, *Proc. Natl. Acad. Sci. U. S. A.*, 2005, **102**, 17907.

9 W. Ludwig, A. Savara, R. J. Madix, S. Schauermann and H.-J. Freund, *J. Phys. Chem. C*, 2012, **116**, 3539.

10 X. Xiao, L. Tao, M. Li, X. Lv, D. Huang, X. Jiang, H. Pan, M. Wang and Y. Shen, *Chem. Sci.*, 2018, **9**, 1970.

11 Y. Liu, S. L. Liu, Y. Wang, Q. H. Zhang, L. Gu, S. C. Zhao, D. D. Xu, Y. F. Li, J. C. Bao and Z. H. Dai, *J. Am. Chem. Soc.*, 2018, **140**, 2731.

12 Z. Pu, I. S. Amiinu, Z. Kou, W. Li and S. Mu, *Angew. Chem., Int. Ed.*, 2017, **56**, 11559.

13 M. Liu, L. Yang, T. Liu, Y. Tang, S. Luo, C. Liu and Y. Zeng, *J. Mater. Chem. A*, 2017, **5**, 8608.

14 C. Zhang, Y. Huang, Y. Yu, J. Zhang, S. Zhuo and B. Zhang, *Chem. Sci.*, 2017, **8**, 2769.

15 W. Zhu, C. Tang, D. Liu, J. Wang, A. M. Asiri and X. Sun, *J. Mater. Chem. A*, 2016, **4**, 7169.

16 E. J. Popczun, C. G. Read, C. W. Roske, N. S. Lewis and R. E. Schaak, *Angew. Chem., Int. Ed.*, 2014, **53**, 5427.

17 C. L. Bentley, M. Kang, F. M. Maddar, F. Li, M. Walker, J. Zhang and P. R. Unwin, *Chem. Sci.*, 2017, **8**, 6583.

18 H. I. Karunadasa, E. Montalvo, Y. Sun, M. Majda, J. R. Long and C. J. Chang, *Science*, 2012, **335**, 698.

19 G. Q. Li, D. Zhang, Y. F. Yu, S. Y. Huang, W. T. Yang and L. Y. Cao, *J. Am. Chem. Soc.*, 2017, **139**, 16194.

20 E. E. Benson, H. Y. Zhang, S. A. Schuman, S. U. Nanayakkara, N. D. Bronstein, S. Ferrere, J. L. Blackburn and E. M. Miller, *J. Am. Chem. Soc.*, 2018, **140**, 441.

21 J. X. Feng, J. Q. Wu, Y. X. Tong and G. R. Li, *J. Am. Chem. Soc.*, 2018, **140**, 610.

22 Y. Cheng, S. Lu, F. Liao, L. Liu, Y. Li and M. Shao, *Adv. Funct. Mater.*, 2017, **27**, 1700359.

23 C. Tsai, H. Li, S. Park, J. Park, H. S. Han, J. K. Norskov, X. Zheng and F. Abild-Pedersen, *Nat. Commun.*, 2017, **8**, 15113.

24 J. Mahmood, F. Li, S. M. Jung, M. S. Okyay, I. Ahmad, S.-J. Kim, N. Park, H. Y. Jeong and J.-B. Baek, *Nat. Nanotechnol.*, 2017, **12**, 441.

25 G. Kresse and J. Furthmuller, *Comput. Mater. Sci.*, 1996, **6**, 15.

26 P. E. Blochl, *Phys. Rev. B: Condens. Matter Mater. Phys.*, 1994, **50**, 17953.

27 G. Kresse and D. Joubert, *Phys. Rev. B: Condens. Matter Mater. Phys.*, 1999, **59**, 1758.

28 J. P. Perdew, K. Burke and M. Ernzerhof, *Phys. Rev. Lett.*, 1996, **77**, 3865.

29 J. M. Soler, E. Artacho, J. D. Gale, A. Garcia, J. Junquera, P. Ordejon and D. Sanchez-Portal, *J. Phys.: Condens. Matter*, 2002, **14**, 2745.

30 J. Junquera, O. Paz, D. Sanchez-Portal and E. Artacho, *Phys. Rev. B: Condens. Matter Mater. Phys.*, 2001, **64**, 235111.

31 N. Troullier and J. L. Martins, *Phys. Rev. B: Condens. Matter Mater. Phys.*, 1991, **43**, 1993.

32 K. N. Mahesh, R. Balaji and K. S. Dhathathreyan, *Int. J. Hydrogen Energy*, 2016, **41**, 46.

33 H. F. Wang and Z. P. Liu, *J. Am. Chem. Soc.*, 2008, **130**, 10996.

34 C. Shang and Z. P. Liu, *J. Chem. Theory Comput.*, 2010, **6**, 1136.

35 S. U. B. Ramakrishna, D. S. Reddy, S. S. Kumar and V. Himabindu, *Int. J. Hydrogen Energy*, 2016, **41**, 20447.

36 *CRC Handbook of Chemistry and Physics*, ed. D. R. Lide, CRC press, 2003–2004.

37 Z. P. Liu, S. J. Jenkins and D. A. King, *J. Am. Chem. Soc.*, 2004, **126**, 10746.

38 C. Shang and Z. P. Liu, *J. Am. Chem. Soc.*, 2011, **133**, 9938.

39 Y. H. Fang and Z. P. Liu, *J. Am. Chem. Soc.*, 2010, **132**, 18214.

40 Y. H. Fang, G. F. Wei and Z. P. Liu, *J. Phys. Chem. C*, 2014, **118**, 3629.

41 J. O. M. Bockris and S. U. M. Khan, *Surface Electrochemistry: A Molecular Level Approach*, Plenum Press, New York, 1993.

42 J. Rossmeisl, A. Logadottir and J. K. Norskov, *Chem. Phys.*, 2005, **319**, 178.

43 C. Shang and Z. P. Liu, *J. Chem. Theory Comput.*, 2013, **9**, 1838.

44 X. J. Zhang, C. Shang and Z. P. Liu, *J. Chem. Theory Comput.*, 2013, **9**, 5745.

45 P. K. Liao, K. E. Spear and M. E. Schlesinger, *J. Phase Equilib.*, 1996, **17**, 340.

46 P. J. Steinhardt, D. R. Nelson and M. Ronchetti, *Phys. Rev. B: Condens. Matter Mater. Phys.*, 1983, **28**, 784.

47 Y. H. Fang and Z. P. Liu, *J. Phys. Chem. C*, 2009, **113**, 9765.

This journal is © the Owner Societies 2018

Phys. Chem. Chem. Phys., 2018, **20**, 27752–27757 | 27757